A Hybrid Beam Steering Free-Space and Fiber Based Optical Data Center Network

Yanwu Liu, Joshua L. Benjamin, Christopher W. F. Parsonson, Georgios Zervas

***Abstract*—Wireless data center networks (DCNs) are promising solutions to mitigate the cabling complexity in traditional wired DCNs and potentially reduce the end-to-end latency with faster propagation speed in free space. Yet, physical architectures in wireless DCNs must be carefully designed regarding wireless link blockage, obstacle bypassing, path loss, interference and spatial efficiency in a dense deployment. This paper presents the physical layer design of a hybrid FSO/in-fiber DCN while guaranteeing an all-optical, single hop, non-oversubscribed and full-bisection bandwidth network. We propose two layouts and analyze their scalability: (1) A static network utilizing only tunable sources which can scale up to 43 racks, $15,609$ nodes and $15,609$ channels; and (2) a re-configurable network with both tunable sources and piezoelectric actuator (PZT) based beam-steering which can scale up to 8 racks, $2,904$ nodes and $185,856$ channels at millisecond PZT switching time. Based on a traffic generation framework and a dynamic wavelength-timeslot scheduling algorithm, the system-level network performance is simulated for a 363-node subnet, reaching $> 99\%$ throughput and 1.23 μs average scheduler latency at 90% load.**

***Index Terms*—Free Space Optics, Data centers, Reconfigurablility.**

I. Introduction

DATA center networks (DCNs) are the main contributors for the growing capacity demand of optical communications [1]. Typically, the global DCN traffic is dominated by communications within data centers (intra-DCNs) stemming from tasks, such as data backup, duplication, reading/writing operations, and the wide usage of parallel programming between distributed and storage nodes [2], [3].

Conventional fiber based DCNs with multiple tiers of switches usually suffer from installation and operational challenges due to high cabling complexity. This leads to long installation times, dusty/lossy connectors, high power consumption, oversubscription, poor scalability, micro-bends and fiber fractures that can lead to network/system outages [4]–[6]. Recent studies of integrating wireless technologies into DCNs have received increasing attention, which can be mainly classified into 2 types: the 60 GHz radio frequency (RF) or Free Space Optics (FSO) [7]. The 60 GHz band RF is a millimeter wave (mmWave) technology that features wide bandwidth (7 GHz) to support the scalability of mega DCNs, short coverage ($\leq$ 15 m) for indoor applications, high power efficiency and low cost transceivers based on 90 nm CMOS technology [7], [8]. Many prior works have proposed either hybrid [9]–[14] or fully wireless [8] DCNs based on 60 GHz interconnects.

FSO is an optical communication technology that mainly utilizes coherent narrow beam laser diodes as light sources and photodetectors as optical receivers to establish highly directional line-of-sight (LOS) links between transceivers, enabling long distance, point-to-point transmissions [15]. Compared with RF technology, indoor FSO offers several advantages suitable for DCN applications, such as less power consumption, license-free, smaller antenna size, immutability against interference and multi-path fading, high-level of security due to inability to penetrate obstacles, higher data rate (Gbps to Tbps) and low path loss ($\sim$ 0 dB for 15 m) [6], [7], [15]–[17]. Compared with optical fibers, FSO provides comparable bandwidth, reduced network installation time, faster propagation speed (1.5 times) and intrinsic immunity from dispersion, birefringence, fiber non-linearities, micro-bends and fractures [7], [18]. These benefits motivate us to integrate FSO technology in DCNs.

The usage of FSO in DCNs has been widely studied. Some focus on the architecture of FSO interconnects in a network level and the associated scheduling algorithms, traffic performances, link budgets, etc. Firefly [6] is a hybrid structure with steerable FSO links installed at top-of-rack (ToR) switches, where they are directed by switchable mirrors or Galvo mirrors and reflected off a ceiling mirror to destinations. In [18], the study proposes a switch-free network, where optical beams from each server within a rack are combined as a FSO-Bus and then directed by a selector. In [19], the study proposes a structure where ToR switches are primarily connected with OM4 fibers and FSO links serve as protections against path failures. In [20], the study introduces an inter-server transceiver, where racks are arranged in a circular layout with ToRs interconnected with a central aggregate switch. In [21], the study proposes the combination of fast wavelength tuning and diffraction gratings at sub-nanosecond switching time. In [22], the study proposes OWCell, where racks are placed at the vertices of a polygon with their ToRs interconnected as a full mesh using fixed line-of-sight (LOS) links with multipoint FSO transceivers [23]. In [24], the study introduces ProjectToR, which is a digital micro-mirror device that can perform beam-steering in tens of thousands of directions in 12 μs reconfiguration time with a reflective "disco-ball" mirror assembly on the ceiling. In [25], the study proposes a photonic integrated circuit transmitter with 2D optical beam steering (OBS) for both inter-rack and inter-cluster communications. Some research focus on improving the compatibility of FSO channels with modulation techniques

The authors are with the Optical Networks Group, Department of Electronic and Electrical Engineering, University College London, London WC1E 7JE, U.K. (E-mail: zczliue@ucl.ac.uk, joshua.benjamin.09@ucl.ac.uk, zciccwf@ucl.ac.uk, g.zervas@ucl.ac.uk)

[26]–[29], relaying techniques [30], rack vibration [31] and intelligent beam alignment control [32]. Some studies focus on FSO interconnects with miniaturised distance (centimeters) to overcome the problems in traditional electrical connectors in high-performance computing and DCNs, such as board-to-board [33]–[35], intra-board [36], intra-chip communications [37], [38], etc.

The majority of aforementioned DCN structures follow a traditional multi-layered switching structure, where FSO channels only serve as extra capacities between ToRs to mitigate hotspots. Inter-node communications are either addressed with conventional switching, or broadcasted by a bus link that requires non-LOS reflections that add to extra multi-hop latency and control difficulties. To address these, we propose a hybrid FSO/fiberd DCN with the following novelties:

1) We propose the physical layer design of a reconfigurable, non-oversubscribed, full-bisection bandwidth hybrid FSO/fibred DCN at its maximum scalability. The topology eliminates tree based multi-layered switching or non-LOS propagation in prior works. Its wavelength reconfigurability is implemented with an all-optical beam-steering switch based on piezoelectric actuators with negligible collimation loss, crosstalk and minimum end-to-end delay (Section II and III).
2) We demonstrate two physical layouts for the FSO DCN: a static layout with sub-nanosecond wavelength tuning sources supporting up to $15,609$ nodes and $15,609$ channels for a mega DCN; or a beam-steering (BS) layout that utilizes both wavelength tuning and FSO switching, supporting up to $2,904$ nodes with a higher bisection bandwidth ($185,856$ channels) at millisecond switching speed (Section IV).
3) We simulate the system-level network performance for the FSO-DCN in a 363-node subnet using on an open-source traffic generation framework and a scheduling algorithm for dynamic wavelength-timeslot reconfiguration, reaching 99.79% throughput with average 1.23 μs scheduler latency at 90% load, similar to that of a previous fibred network PULSE (64-node, 99.79% throughput, 0.91 μs average latency). The FSO subnet could greatly increase the network size without significantly degrading the scheduler performance, with further benefits from replacing fibres with FSO including reduced propagation delay, reduced cabling complexity, elimination of fibre nonlinearities and a full-bisection bandwidth brought by FSO switches (Section V).

II. Proposed Architecture

The proposed DCN is built on an existing intra-DCN known as 'PULSE [39]. PULSE is a single hop, optical circuit switching DCN at nanosecond reconfiguration time, built from parallel broadcast-and-select subnets, fast tunable transceivers and a novel hardware-based wavelength-timeslot scheduler, scaling up to 4096 nodes with a capacity of 25.6 Pbps across 260k optical channels [39], [40]. Inspired by PULSE, our proposed DCN features physical topology reconfigurability with piezoelectric actuator based FSO beam steering.

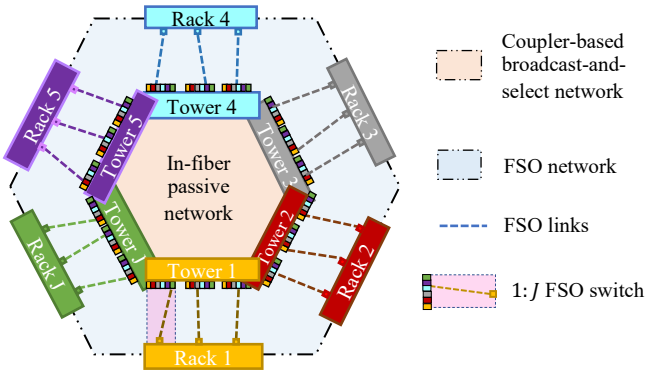

Fig. 1. A top view of the polygon DCN with J racks.

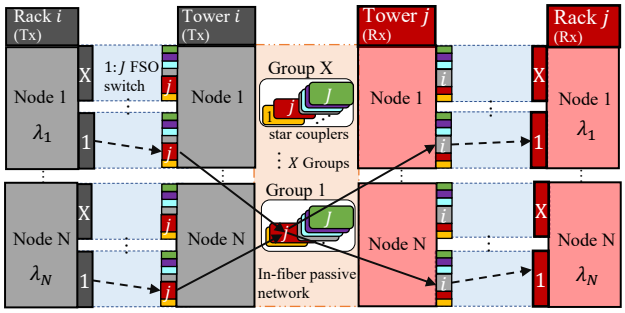

Fig. 2. An unfolded communication. The 1^{st} transmitter in each node in Rack i are connecting to the 1^{st} receiver in each node in Rack j through the j^{th} star coupler in Group 1. $i = j$ for intra-rack communication and $i \neq j$ for inter-rack communication ($i, j \in J$). Dashed lines represent reconfigurable links within each FSO switch. Solid lines represent fixed fiber connections between star couplers and FSO end collimators. Simultaneous connections between other transceivers are omitted for simplicity.

TABLE I
Parameters Summary for Fig. 2

Parameter	Symbol
Racks per DCN	J (even)
Nodes per rack	N
Transceivers per node per rack	$X = J\,2^p$
FSO switches per Transceiver	2
FSO switch ratio	$1:J$
Towers per DCN	J
Star coupler dimension	$N \times N$
Loss per star coupler [39]	$-3\log_2 N$
Star couplers per DCN	J^2X
$1:J$ FSO switches per DCN	$2NXJ$
Wavelengths per star coupler	N

Fig. 1 shows a top view of our proposed DCN. Together, the racks form an outer polygon, where each rack is assigned with a dedicated tower located at the inner polygon. The towers are interconnected as a coupler-based in-fiber passive network. In any communication, either intra- or inter-rack, the information is first sent by a source rack to its exclusive tower via FSO links, and then propagated through the fiber network to the destination tower, and eventually received by the destination rack via FSO links.

Fig. 2 shows a high-level network structure between any

TABLE II
PARAMETERS SUMMARY FOR FIG. 3 AND FIG. 4

Parameter		Symbol
Blue Collimators (Tx) at Rack i, Side x, Cell c, Node n		$\mathfrak{T}_{i,x,c,n}$
Red Collimators (Rx) at Rack j, Side x, Cell c, Node m		$\mathfrak{R}_{j,x,c,m}$
Tx (or Rx) Collimators per node per rack		$X = J2^p$
Tx (or Rx) Collimators per node per tower		XJ
Sides per rack (or tower)		J
Cells per side per rack (or tower)		2^p
Star Coupler	Inputs (N nodes): Tower i, Side x, Cell c, Column j	$\mathbb{T}_{i,x,c,j}$
	Outputs (N nodes): Tower j, Side x, Cell c, Column i	$\mathbb{R}_{j,x,c,i}$
where $i \in J$, $j \in J$, $x \in J$, $c \in 2^p$, $n \in N$, $m \in N$		

two racks and their towers. For the sake of clarity, we define a list of symbols and their physical meanings in Table I. A DCN contains a total of J racks. Each rack vertically contains N nodes. Each node horizontally contain X transceivers ($X = J2^p$, where p can be any non-negative integer, $0, 1, 2, ...$). Each transceiver contains two FSO switches, one for transmission (Tx) and one for reception (Rx). Each FSO switch exhibits a $1 : J$ ratio, which contains one collimator on the rack performing beam steering to select from J end collimators on the tower.

Regarding the in-fiber passive network, each tower is built from XJ star couplers each in a $N \times N$ dimension. Each star coupler connects to 1 of the J ends in a FSO switch from all N nodes. Therefore, a group of J star couplers can route to J different racks and there are X such star coupler groups assigned to X transceivers in an one-to-one correspondence. Upon communication, as the highlighted path shown in Fig. 2, each transmitter on the source (i.e., Rack i) performs a $1 : J$ FSO switching to select a star coupler whose index represents the destination (i.e., Rack j). Each star coupler broadcasts signals from all the nodes using N different wavelengths. Similarly, each receiver on Rack j also performs a $1 : J$ FSO switching to select 1 out of J sources. For simplicity, we only allow a single ray communication between 2 collimators facing exactly at each other. Multiple incident rays onto a single collimator are not considered. Any beam steering is limited in the horizontal direction within the $1 : J$ FSO switch, whereas the vertical direction only serve the purpose of vibration corrections.

Fig. 3 demonstrates the physical structure of a single rack and its tower. Note that the real dimensions should be doubled since only Txs is drawn and Rxs is an exact duplicate installed beside. The rack is further divided and labeled into J sides. Similarly, the tower is also divided into J sides, each assigned to the rack sides in a one-to-one correspondence, as denoted in the dashed lines. However, due to the FSO switches, the tower is always J times larger in the number of collimators than the rack. Both rack and tower exhibit a near semicircle structure and details will be discussed more in Section IV-C.

The routing logic that guarantees a full-bisection bandwidth is introduced as follows. We summarize a list of notations in

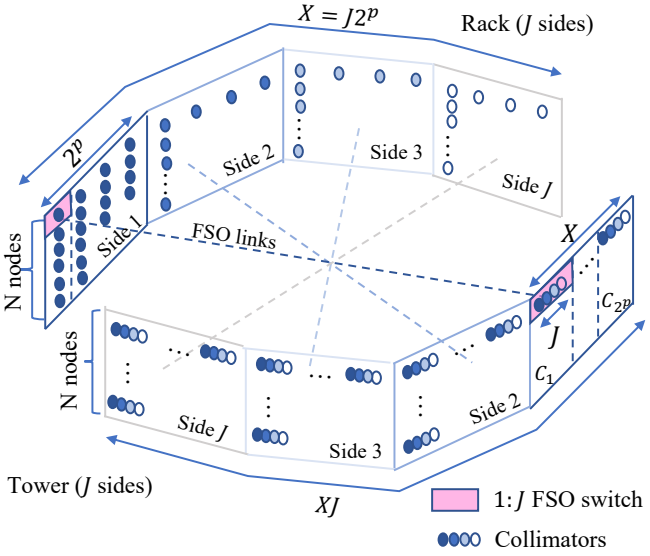

Fig. 3. The physical structure of a rack and its tower (Txs only. Rxs is a duplicate installed beside, see Appendix B, Fig. 17).

Table II. Fig. 4 demonstrates the unfolded physical structure between a source Rack i, Side x and a destination Rack j, Side x, where $i, j, x \in J$. We further divide each side into smaller cells labeled as C_c, where $c \in 2^p$. Each cell is assigned with a dedicated group of J star couplers, where each star coupler is in a $N \times N$ dimension using N different wavelengths that connects to one column in the tower cell from all the nodes. On the Txs tower (blue), the input column of any star coupler can be denoted as Tower i, Side x, Cell c, Column j (for simplicity this is only shown as $\mathbb{T}_j$ on the figure). The output column of this star coupler should be placed at Tower j, Side x, Cell c, Column i (shown as $\mathbb{R}_i$) on the RX tower (red). An end-to-end routing between any node on any rack (i.e., $\mathfrak{T}_{i,x,c,n} \rightarrow \mathfrak{R}_{j,x,c,m}$) is given as,

$$\text{Tx Collimator: } \mathfrak{T}_{i,x,c,n} \tag{1a}$$
$$\text{FSO beam steering to: } \mathbb{T}_{i,x,c,j} \text{ , at Node } n \tag{1b}$$
$$\text{Star coupler broadcasts to: } \mathbb{R}_{j,x,c,i} \text{ , at all Nodes} \tag{1c}$$
$$\text{Rx Collimator: } \mathfrak{R}_{j,x,c,m} \tag{1d}$$

Restricted by this topology, any free routing only involves the index changes between racks ($i \rightarrow j$) and nodes ($n \rightarrow m$) by wavelength selection, whereas the side and cell (x and c) remain unchanged. The highlighted path in Fig. 4 indicates that $\mathfrak{T}_{3,x,1,1}$ is communicating with $\mathfrak{R}_{2,x,1,1}$, where x can be any value since networks formed between each pair of sides are independent. It is also possible for different nodes within the same cell route to different racks using different star couplers since each FSO switch is also independent and a resource scheduler aforementioned [40] must synchronize between transceivers.

In summary, the key novelties of our proposed DCN include: (1)The $1 : J$ FSO switch allows every transmitter to select freely from one of the J destination racks. Similarly, every

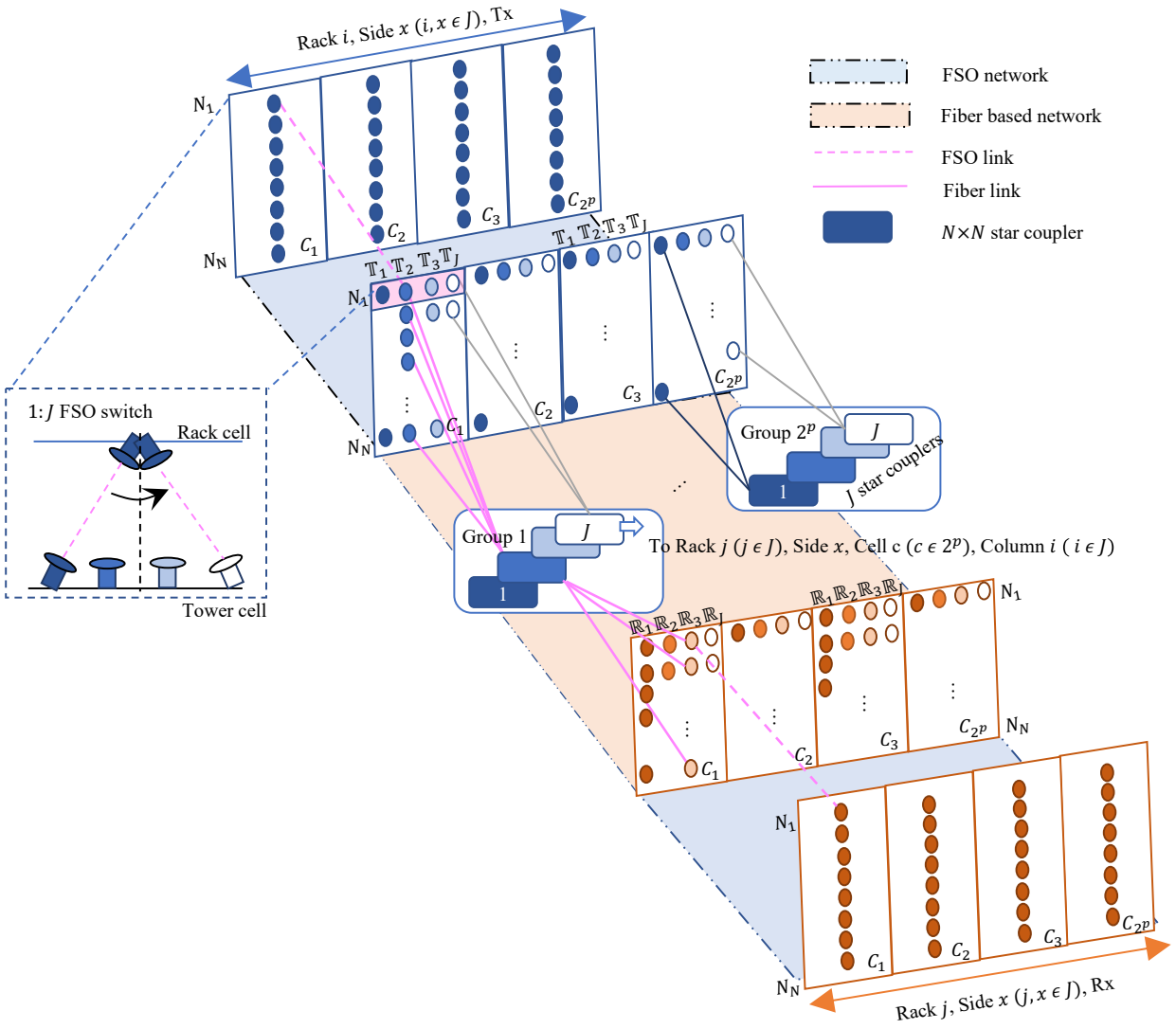

Fig. 4. An unfolded structure from a source Rack i, Side x to a destination Rack j, Side x. The highlighted route indicates $i = 3$, $j = 2$, since $\mathbb{T}_2$ and $\mathbb{R}_3$ are in use.

receiver is able to freely select one from the J source racks. This guarantees a full bisection bandwidth of $\frac{NXJ}{2}$, which can be strictly non-blocking without wavelength contention, as long as there are N different wavelengths on the same star coupler. (2) When $p > 0$ and $X > J$, the additional cells within each side can be regarded as an independent duplication of C_1 and this ensures strong tolerance against link failures. (3) Instead of scanning across the entire rack, when X is fixed and p increases, the tower is divided into smaller cells so that the required horizontal beam steering angle is correspondingly reduced. In the following section, we describe the geometry of this FSO switch and its point-to-point link performance.

III. FSO Switching Geometry

The piezoelectric effect describes a linear relationship where a mechanical displacement can be generated in response to an applied electrical signal [41]. Piezoelectric actuators (PZT) based optical beam-steering is a mature solution for DCNs in commercial products, such as POLATIS [42], which supports a maximum 384×384 non-blocking all-optical switch with position sensors and precise feedback control against hysteresis and vibrations. Inspired by POLATIS, we propose the PZT based $1 : J$ FSO switch. As shown in Fig. 5, we assume that each collimator is always fixed to a fiber as a fiber-collimator package. A PZT is attached to the fiber on either axis of the $x - y$ plane to move the entire package as a 2D switch. We denote the collimator radius as r, the maximum achievable actuator angle as α, the total device length after installing the collimator onto the fiber to the pivot as $L\,(L \geq r)$. The minimum gap G between adjacent collimators is therefore given by

$$G = \begin{cases} 2\left(r\cos\alpha + L\sin\alpha\right), & 0 < \alpha \leq \frac{\pi}{2} - \operatorname{atan}\left(\frac{r}{L}\right), \\ 2\sqrt{r^2 + L^2}, & \frac{\pi}{2} - \operatorname{atan}\left(\frac{r}{L}\right) < \alpha < \frac{\pi}{2}. \end{cases} \quad (2)$$

The FSO link is simulated assuming an ideal monochromatic Gaussian beam built on the ray tracing model reported in [43]. Fig. 6 shows a point-to-point link where two thin lenses are installed at their focal distance f from Tx and Rx

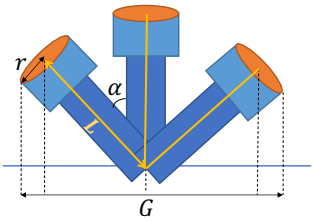

Fig. 5. Required gap between adjacent collimators in one axis ($L \geq r$).

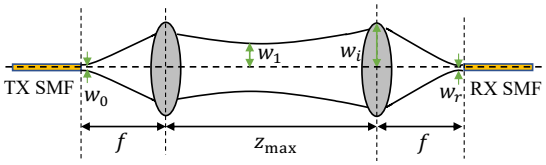

Fig. 6. Point-to-point FSO link.

single-mode fiber (SMF), respectively. We define w_0 as the initial mode field radius, λ as the beam wavelength and w_1 as the beam radius after Tx collimation. The Rayleigh range of w_1 is used as the maximum free space distance $z_{\max}$ between the two lenses [44],

$$z_{\max} = \frac{\pi w_1^2}{\lambda} = \frac{f^2 \lambda}{\pi w_0^2}\,. \tag{3}$$

Many prior studies have shown that indoor FSO links can achieve near lossless [45] or seamless transmission [46]. Specific to this work, the aim is to find the optimal parameters r and α that maximize FSO-DCN physical scalability while maintaining a worst case performance of collimation loss. We assume a fixed fiber-collimator package where any relative angular misalignment will only occur between the optical axes of the two lenses. The resultant collimation loss L_{colm} is the sum of Rx fiber coupling with an offset [47] captured by L_{offset} term and beam clipping L_{clip} at Rx lens [48], given as

$$L_{\text{colm}} = L_{\text{offset}} + L_{\text{clip}}\,, \tag{4}$$

where

$$L_{\text{offset}} = -10\log_{10}\left\{\left(\frac{2w_r w_0}{w_r^2 + w_0^2}\right)^2 \exp\left(-\frac{2d^2}{w_r^2 + w_0^2}\right)\right\}, \tag{5}$$

and

$$L_{\text{clip}} = -10\log_{10}\left\{\exp\left(-\frac{2\zeta^2}{w_i^2}\right) \cdot \sum_{k=0}^{\infty}\left[\frac{2^k \zeta^{2k}}{w_i^{2k} k!}\left(1 - \exp\left(-\frac{2r^2}{w_i^2}\right)\sum_{n=0}^{k}\frac{2^n r^{2n}}{w_i^{2n} n!}\right)\right]\right\}, \tag{6}$$

where r is the radius of the Rx lens, w_i, w_r are the incident beam radius at the Rx lens and the Rx fiber, respectively. ζ, d are the lateral offset of the beam center from the lens and the fiber center, respectively.

Three link designs centered at 1550 nm are tested with their $z_{\max}$, required focal lengths, Tx/Rx lens diameter, PZT misalignment tolerance summarized in Table III. As shown in Fig. 7, each link is sufficient to cover a near lossless collimation for a full $(C+L+S)$−band. These link parameters determine the physical dimension of a FSO-DCN, which will be analyzed in the next section.

TABLE III
PROPOSED LINK DESIGNS AT 1550 NM WAVELENGTH

$z_{\max}$ [m]	**Focal length** [mm]	**Diameter** [mm]	α **Tolerance** [deg]
4	14.81	5.5	3.0×10^{-3}
5	16.56		
6	18.14		

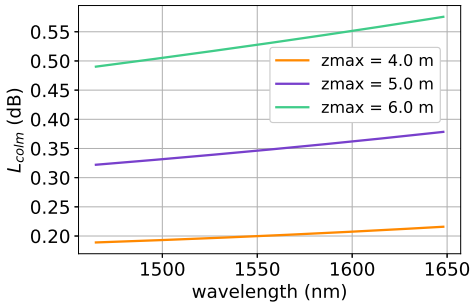

Fig. 7. Total collimation loss (L_{colm}) at RX collimator and fiber for different wavelengths under 3 link designs.

TABLE IV
PARAMETER SCAN RANGE FOR THE STATIC AND THE BEAM-STEERING LAYOUT

Layout	α [deg]	$2r$ [mm]	L [mm]	$z_{\max}$ [m]
Static	3.0×10^{-3}	[5.5, 20]	[10, 60]	4, 5, 6
Beam-steering	$[3.0 \times 10^{-3}, 90]$			

IV. Dimension and Scalability

This section introduces two physical layouts for the proposed DCN: a static layout that does not allow any beam-steering with FSO only used as a replacement of fibers and PZT only used for angular error calibration; and a beam-steering layout that allows FSO switches up to J. The parameter range in both simulations are listed in Table IV.

A. Fast tunable transmitter design

To avoid wavelength contention in star couplers, the reconfigurability in both layouts needs an additional wavelength routed optical switching. The work in [49] demonstrated a hybrid wavelength tunable source (WTS) using a pair of digital supermode distributed Bragg reflector (DS-DBR) lasers and semiconductor optical amplifiers (SOAs) with AI-aided optimized driving signals in [50], experimentally demonstrating a continuous tuning of 122×50 GHz between $1524.11 - 1572.48$ nm with < 900 ps switching time. With three such WTSs combined together as a single transmitter, this fast tunable source is able to support more than 300 wavelengths in a full $(C+L+S)$−band at sub-nanosecond switching time, which is sufficient to cover both layouts.

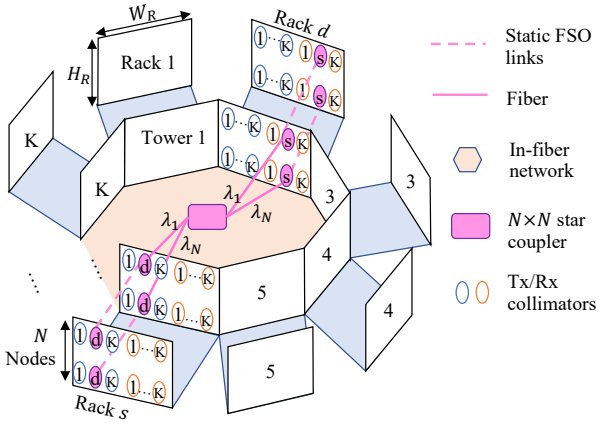

Fig. 8. Overall structure for FSO-ST with K racks. The inputs of an arbitrary star coupler are denoted as Tower s, Column d. Its outputs are placed at Tower d, Column s, where $\{s, d\} \in K$.

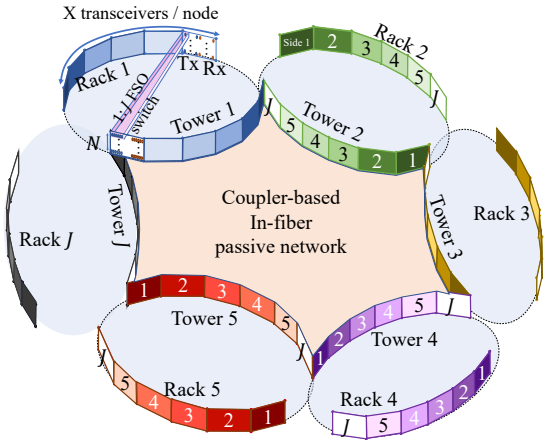

Fig. 9. Overall structure for FSO-BS with J racks. The details of each rack and its tower are shown in Fig. 3. The details of the coupler-based in-fiber network are shown in Fig. 4.

B. Static Layout

The static layout (FSO-ST) does not implement beam steering in any direction and the design reduces to a static DCN named as "PULSE" [39], [51], [52]. As shown in Fig. 8, since there is no need for FSO switches, a tower reduces to the same height, width and scalability as a rack, each housing $N \times 2K$ collimators. Following a same topology as PULSE, FSO-ST can scale up to K racks and K towers. Within each node, there is only one fast tunable transmitter (as in Section IV-A), where its output is split into K different wavelengths, each sent to a collimator. Upon transmission, as the highlighted path in Fig. 8, only 1 of the K (i.e., the d^{th} Tx collimator) in every node on the source rack R_s is switched on, propagated through the static FSO links, broadcasted by the d^{th} star coupler (using N different wavelengths to avoid contention), routed to the destination rack R_d and received by the s^{th} Rx collimator tuned to the same wavelength, i.e., $\{s, d\} \in K$. It is also possible for different nodes within the same rack tuning to different destinations.

Regarding its scalability, FSO-ST still requires the usage of actuators to reduce pointing errors. The value of K and N are calculated as $K = \lfloor \frac{W_R}{2G} \rfloor$, $N = \lfloor \frac{H_R}{G} \rfloor$, where $\lfloor \cdot \rfloor$ represents the floor function, $W_R = 482.6$ mm (a standard rack width), height $H_R = 2$ m, G is calculated with Table IV using (2). For simplification, the correlation between focal length and collimator radius upon manufacturing is ignored. The maximum scalability is $N_{\max} = 363$ and $K_{\max} = 43$ (See Fig. 16, Appendix A). Therefore, FSO-ST could scale up to 43 racks, with a total of $N \times K = 15609$ nodes, and thus 15609 channels.

C. Beam-steering Layout: Switching across FSO links

The beam-steering layout (FSO-BS) allows FSO switches in horizontal direction for each transceiver to connect up to J. Therefore, FSO-BS is equivalent to the structure shown in Section II. A fast tunable transmitter that supports > 300 wavelengths (in Section IV-A) is installed behind every Tx collimator on the rack. As shown in Fig. 9, racks and towers

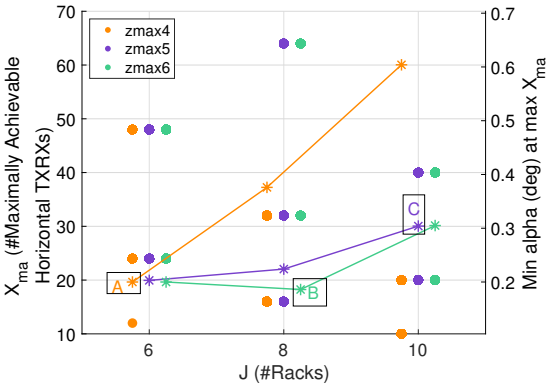

Fig. 10. Left axis: Maximally achievable horizontal transceivers X_{ma} for FSO-BS hosting J racks. Right axis: Minimum required α (deg) at maximum X_{ma} against J.

are reshaped into arcs located symmetrical on a circle. The entire DCN consists of J such Rack-Tower circles, each located on one of the J edges of a central polygon that contains the in-fiber passive network.

For each combination of $\{\alpha, r, L, z_{\max}\}$ in Table IV, the physical feasibility, such as blocking, overlapping, beam-steering coverage is verified (see Appendix B). Among all feasible sets, we aim to find the maximally achievable X (denoted as X_{ma}), where X represents the number of transceivers per node per rack. A summary is plotted in Fig. 10. The left axis is a scatter plot where each circle represents X_{ma} for a DCN hosting J racks. The right axis is a line plot where each asterisk represents the minimum required α [deg] for each J to reach the maximum X_{ma}.

In this case, to build a FSO-BS under each value of J, we highlight 3 points A, B, C since they provide the least α required at the maximum X_{ma}. Their parameters are summarized in Table V. Since there is no beam steering in the vertical direction, $N_{\max} = 363$, same as that in FSO-ST. The top views of the entire DCN for case A, B, C are plotted in Fig. 11 (a-c), respectively. The x and y axis represent the

TABLE V
PARAMETERS SUMMARY FOR HIGHLIGHTED POINTS

	D [mm]	L [mm]	$z_{\max}$ [m]	J	p	α [deg]	X	N	Total channels (JXN)
A	5.5	12	4	6	3	0.200	48	363	104,544
B	5.5	10	6	8	3	0.186	64	363	185,856
C	5.5	37	5	10	2	0.304	40	363	145,200

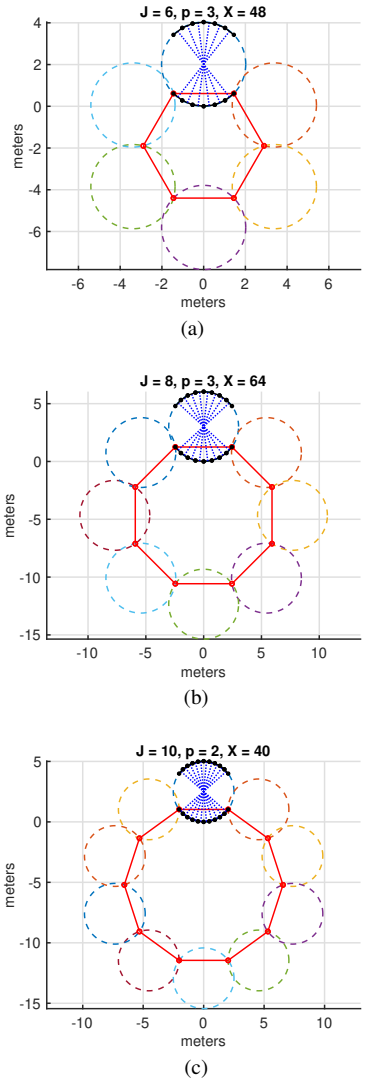

Fig. 11. Top views for $J = 6$, 8 and 10-rack DCN.

TABLE VI
TRAFPY TRAFFIC GENERATION SETTINGS

Parameter	Value
# Nodes per subnet (N)	$\{363, 64\}$
Node-to-node capacity (C)	400 Gbps
Overall Load (η)	$\{50\%, 70\%, 90\%\}$

coordinates in meters. The black arcs highlight 1 of the J Rack-Tower pairs.

TABLE VII
SCHEDULER SETTINGS

Parameter	Value
Timeslot duration (t)	20 ns
Wavelength reconfiguration	Slot-level
#Timeslots per epoch (L)	4
Epoch duration (E)	80 ns
#Total epochs	Varies, see Fig. 12
#Average requests/epoch/node (R)	2

V. NETWORK SIMULATION

A. Scheduler performance

This section introduces a network simulation of a hardware dynamic wavelength-timeslot scheduler (DSU) to assess the system-level performance of FSO DCN at its maximum dimension. The simulation follows a two step process where a traffic pattern is first generated using Trafpy [53] and then sent to the DSU in MATLAB. Trafpy is an open access benchmarking framework in Python capable of generating any pattern for any network in any simulation environment. Due to parallelism, the system-level performance across the entire DCN is same as a N-node subnet consists of a $N \times N$ star-coupler that connects uni-directionally between two racks. Each node is split into a source and a destination and the maximum node-to-node capacity is assumed 400 Gbps. As shown in Table VI, we simulate two subnets: FSO-DCN ($N = 363$) and PULSE ($N = 64$) at 3 different loads: $\eta = 0.5$, 0.7 and 0.9, where each load represents generated demands that totally request for the corresponding fraction of maximum total subnet capacity across the duration of all demands. Each demand consists of: information flow size (sampled from a Weibull distribution), event time (with a constant inter-arrival rate), and source-destination (SD) pair. The generated traffic is skewed with random hot/cold nodes as shown in Fig. 12 with detailed distribution described in Appendix C. Finally, we repeatedly generated each traffic $\{N, \eta\}$ with three seeds to average out randomness.

The traffic demands are then sent to the DSU scheduler which parallelises and translates them into the number of timeslots and epochs required across each node, according to the settings in Table VII. An independent DSU scheduler utilises N wavelengths per subnet and reconfigures wavelength assignment for each node at every $t = 20$ ns timeslot. Every $L = 4$ timeslots are grouped together as an epoch ($E = 80$ ns) defined as the circuit reconfiguration time. Each request contains the number of timeslots needed for each flow. During each epoch, DSU performs up to I iterations to assign wavelengths and timeslots to each request, whereas failed or partially granted requests after I attempts are then buffered in the scheduler to retry in the following epochs. The performance of the DSU scheduler is shown in Fig.13. The throughput is defined as the $granted/requested$ timeslots within the total length of epochs. The average scheduler latency is the duration of requests to be granted by DSU, whereas dropped requests (if not granted by the end of total epochs) do not count. Without considering actuator beam-

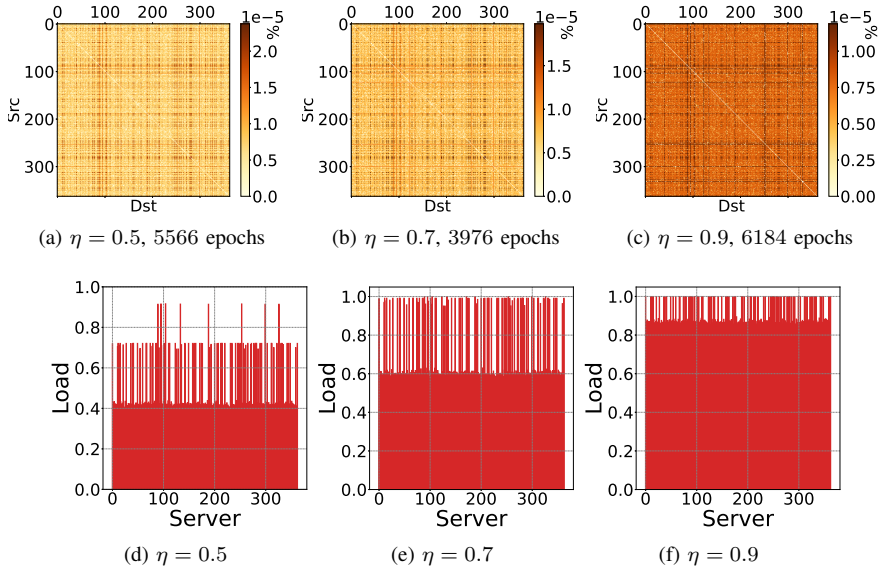

(a) $\eta = 0.5$, 5566 epochs (b) $\eta = 0.7$, 3976 epochs (c) $\eta = 0.9$, 6184 epochs

(d) $\eta = 0.5$ (e) $\eta = 0.7$ (f) $\eta = 0.9$

Fig. 12. Seed 1: (a-c) Percentage of each source-destination pair over the total load of the N-363 subnet. (d-f) Individual load on each node (considering both source and destination) over its capacity, approaching a uniform distribution as η approaches 1.0.

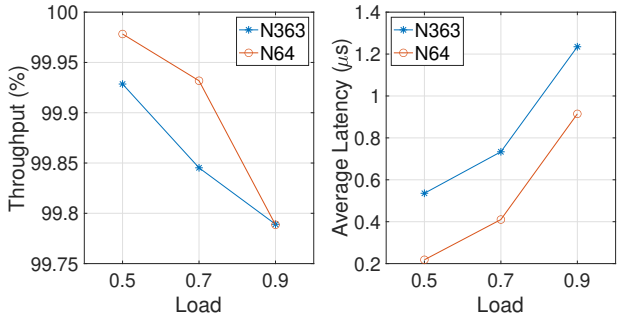

Fig. 13. Scheduler performance of throughput and average latency for FSO-DCN (N-363) and PULSE (N-64) under $\eta = 0.5$, 0.7 and 0.9.

steering latency in FSO switches (as will be discussed separately in Appendix D), the scheduler algorithm is identical for both FSO layouts and the fibred PULSE, thereby identical control and configurations times for all three structures. Comparing between two subnets, N-363 at 0.9 load reaches 99.79% throughput, 1.23 μs average delay, whereas N-64 at 0.9 load reaches 99.79% throughput, 0.91 μs average delay. This indicates that the throughput is almost constant ($< 1\%$ reduction) as both subnet size and load increases, whereas the average latency do not significantly increase as subnet size. The complementary cumulative distribution functions (ccdf) of scheduler latency across all epochs and all nodes are shown in Fig. 14. At N-363 and 0.9 load, the subnet has a worst case of 5.76 μs tail (99th percentile), 1.28 μs median, and a best case of 2.38 μs tail, 0.86 μs median. For N-64 and 0.9 load, the worst case is 2 μs tail, 1 μs median, and a best case of 1.62 μs tail, 0.76 μs median.

B. Propagation latency

Fig. 15 shows the propagation latency in data plane for PULSE, FSO-ST ($N = 363$, $K = 43$) and FSO-BS (Fig.11b). In PULSE, we assumed L meters of fiber from source rack to the coupler and L meters from the coupler to destination, where $L = 3$ m and 20 m for intra-rack and intra-cluster (i.e., inter-rack) communications, respectively [39]. In FSO-ST, we assume $2 * z_{\max} = 12$ m in FSO and $W_R/2 = 0.24$ m in fiber for intra-rack; 12 m in FSO and 6.61 m (diameter of a regular $43-$polygon with W_R as one side) for intra-cluster. In FSO-BS, we assume 12 m in FSO and $W_{\text{TS}}/2 = 0.36$ m in fiber for intra-rack; 12 m in FSO and 12.8 m (diameter of tower polygon) for intra-cluster. Inter-cluster communications are not considered. At a similar physical scale, both FSO layouts demonstrate a reduction in intra-cluster delay than the fibred PULSE.

C. Comparison between two FSO layouts and PULSE

Table VIII summaries the comparison between FSO-ST and FSO-BS. Benefiting from the $1 : J$ FSO switch, FSO-BS supports a bisection bandwidth 10 times more than FSO-ST. Both layouts can operate with negligible crosstalk, since the largest beam diameter spreading (at $z_{\max} = 6$ m) incident on RX lens is still smaller than the minimum lens diameter (5.5 mm) so that adjacent channels do not overlap spatially, nor spectrally. The indoor environment is free from atmospheric

TABLE VIII
COMPARISON BETWEEN STATIC AND BEAM-STEERING LAYOUT DCNS

	FSO-ST		**FSO-BS**		**PULSE [39]**	
Type	Hybird FSO/Fiber		Hybird FSO/Fiber		Fiber	
Architecture	Fig. 8		Fig. 9		[39, Fig. 1]	
Reconfigurability	Wavelength Routing		FSO Beam-steering & Wavelength Routing		Wavelength Routing	
Link Direction (per subnet)	Uni-directional		Unii-directional		Uni-directional	
Scheduler Delay	Sub to microseconds		Sub to microseconds		Sub-microseconds	
Propagation Delay	Sub-microseconds		Sub-microseconds		Sub-microseconds	
Wavelength Switching Delay (see Appendix D)	Sub-nanoseconds		Milliseconds and/or sub-nanoseconds		Sub-nanoseconds	
Dimension	Symbol	Max	Symbol	Max (Case B)	Symbol	Max
# Racks	K	43	J	8	U	64
# Nodes per Rack	N	363	N	363	U	64
# Transceivers per Node	-	1	X	64	U	64
# FSO links (reduced fibers)	$2NK$	$31,218$	$2NXJ$	$371,712$	-	
Bisection bandwidth(#channels)	$NK/2$	$7,804$	$NXJ/2$	$92,928$	$U^3/2$	$131,072$
# Wavelengths required to be contention-free	N		N		U	

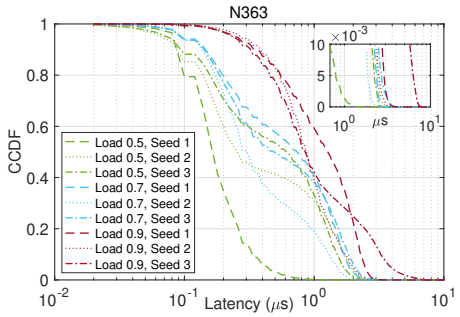

(a)

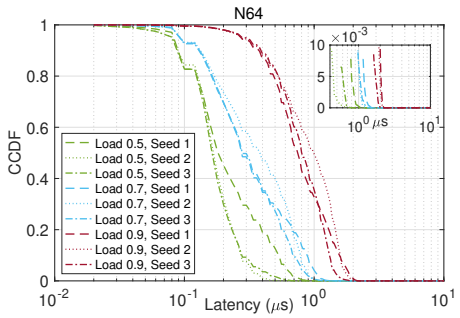

(b)

Fig. 14. Scheduler latency CCDF distribution for (a) N-363 and (b) N-64 subnet. Inset: 99th percentile.

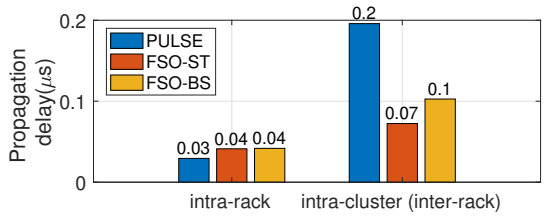

Fig. 15. Data plane propagation delay of PULSE, FSO-ST and FSO-BS.

turbulence induced absorption, fading or scattering [54]. In classical electrodynamics, intersections of FSO links in vacuum do not affect each other since there is no elastic photon-photon scattering involved [55], [56].

Finally, we compare both layouts with the fully fiberd DCN PULSE. FSO links are transparent to modulation formats and baud rates such that all three DCNs can reach the same per channel capacity. The network simulation with the revised scheduler shows a marginally stable performance as the subnet size expands from 64 to 363 with extra benefits from FSO replacing fibre connections, including a significant reduction of cabling complexity, intrinsic immunity against fiber nonlinearities, faster propagation speed in free space and a full-bisection bandwidth. The experimental prototype of FSO switching will be addressed in a future work. Currently, a practical analysis regarding PZT usage is shown in Appendix D.

VI. CONCLUSION

This paper presents a reconfigurable, non-oversubscribed, hybrid FSO/fiber intra-DCN architecture with a full-bisection bandwidth. The novelty of this paper focuses on the physical layer design, where we present two DCN layouts: (1) A static layout with fixed FSO links that scales up to 43 racks and $15,609$ and (2) A beam-steering layout that scales up to 8 racks, $2,904$ nodes and $185,856$ channels. A system-level simulation based on a traffic generation framework and a revised scheduler is performed for a 363-node FSO subnet, reaching $> 99\%$ throughput, 1.23 μs average scheduler latency at 0.9 load. The FSO subnet could greatly increase the network size than the fibred 64-node PULSE without significantly degrading scheduler performance. The FSO subnet also shows reduced propagation delay and cabling complexity benefiting from FSO replacing fibres, as well as a full bisection bandwidth due to the $1:J$ FSO switch.

In summary, this paper highlights the importance and potential of a hybrid FSO/fiberd DCN. Future works would

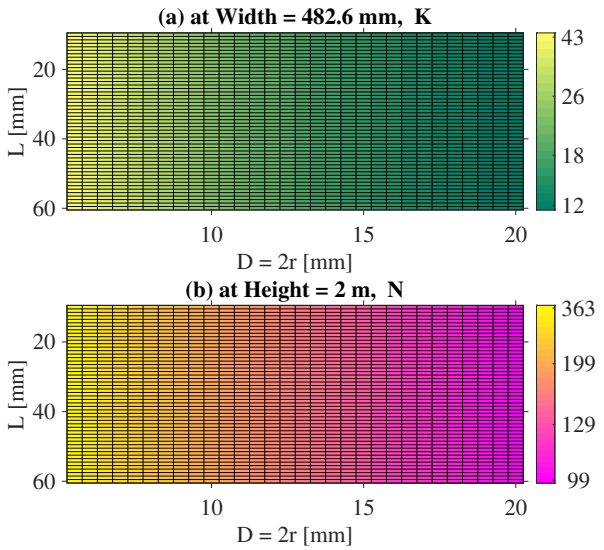

Fig. 16. Heatmap of (a) horizontal transceiver pairs (K) can be hosted in $W_R = 482.6$ mm. (b) vertical servers (N) can be hosted in $H_R = 2$ m.

be focused on implementation of suitable actuators, control analysis, cost analysis and physical experiments on the proposed structure to verify current results presented.

Funding. This work was supported under the Engineering and Physical Sciences Research Council OptoCloud (EP/T026081/1), and the TRANSNET (EP/R035342/1) grants as well as the the Industrial Cooperative Awards in Science and Technology co-funded by British Telecom.

Disclosures. The authors declare no conflicts of interest.

APPENDIX A
STATIC LAYOUT

Fig.16 demonstrates the heatmap of K and N for a static layout by scanning across the parameters in Table IV. On x-axis, the centre of each pixel labels lens diameter $D = 2r$ from 5.5 mm to 20 mm, at a gap of 0.5 mm. Y-axis labels device length L from 10 to 60 mm, at a gap of 1 mm. z_{max} does not affect the scalability in the static layout.

APPENDIX B
BEAM-STEERING LAYOUT

Fig. 17 demonstrates a top view between a single side of the rack and a single side of the tower. On the rack, each collimator is installed at the center of the cell and requires a beam steering angle $\pm\theta$ and FSO link distance of z_{max} to reach either edge collimator of the tower cell. On the tower, each collimator is evenly spaced at G and x_1 is the horizontal distance between the centre of the cell and its end collimator. We denote the width of a tower side as W_{TS}, the width of a rack side as W_{RS}. S is the perpendicular distance in-between.

A rack consists of J such sides in Fig. 17. As shown in Fig. 18, a complete rack and a tower are symmetrically located on either half of a circle. Each side (W_{RS} or W_{TS}) still maintains as a flat surface. Intrinsically, a pair of W_{RS} and W_{TS} should always be parallel against each other.

Therefore, this raises a feasibility problem. We denote α as the maximum angle provided by an actuator, R_{rtc} as the radius of the rack-tower circle, O and O' as the center of the circle and its neighbor, Υ as half of the central angle of a single side. For each parameter combination of $\{r,\, L,\, z_{\max},\, \alpha\}$ in Table IV, we need to ensure the physical feasibility with respect to the problem in (7): the required angle is less than actuator angle; the arc of either rack or tower does not exceed half of the circle; and the adjacent circles do not overlap inside the tower polygon. Finally, among all the feasible combinations, we select the one that yields maximum integer value of $X = J\,2^p$, where X is the number of transceivers per node per rack, J is the number of racks in a DCN and $J = \{n \in \mathbb{Z}^+ : n \geq 4\}$, and p is a non-negative integer ($p \in \mathbb{Z}_{\geq 0}$). Mathematically, this problem is formulated as,

$$\max_{r,\, L,\, z_{\max},\, J,\, p,\, \alpha} \quad X\,, \tag{7}$$

$$\text{s.t.} \quad \theta \triangleq \operatorname{asin}\left(\frac{x_1}{z_{\max}}\right) \leq \alpha\,, \tag{8a}$$

$$2\left(\frac{\pi}{2} - J\Upsilon\right) + \frac{(J-2)\,\pi}{J} \geq \pi\,, \tag{8b}$$

$$\Upsilon \triangleq \operatorname{atan}\left(\frac{W_{\mathrm{TS}}}{S}\right) \leq \frac{\pi}{2J}\,, \tag{8c}$$

where the following notations have been introduced:

$$x_1 \triangleq \frac{(J-1)\,G}{2}\,, \tag{9a}$$

$$S \triangleq \sqrt{z_{\max}^2 - x_1^2}\,, \tag{9b}$$

$$W_{\mathrm{TS}} = 2J\,2^p\,G\,. \tag{9c}$$

For each combination of $\{r, L, z_{\max}\}$, Fig. 19 and Fig. 20 demonstrate the maximum achievable X (denoted as X_{ma}) and corresponding required α [deg], J and p. On x-axis, the centre of each pixel labels lens diameter $D = 2r$ from 5.5 mm to 20 mm, at a gap of 0.5 mm. Y-axis labels device length L from 10 to 60 mm, at a gap of 1 mm. A summary of these two plots is given in Fig. 10 (See Section IV-C).

APPENDIX C
TRAFPY AND SCHEDULER SETTINGS

Upon generation of a skewed traffic defined by N, η, Trafpy firstly selects a value $K \sim U(0.1N, 0.3N)$ as the number of skewed nodes, where U represents a uniform distribution. Each skewed node has a probability of $n_k \sim U(0.5/K, 0.8/K)$, $k \in K$. Then, Trafpy generates a $N \times N$ distribution matrix containing the probability of each source-destination (SD) pair , where self-connections are not considered. Each skewed pair (g, h) with at least one skewed node has a probability $p_s = (n_g + n_h)/2(N-1)$, where $n_g, n_h = n_k$ if $g, h \in K$, otherwise $= 0$). The remaining are unskewed pairs each assigned with a probability p_u sampled from a multinomial distribution with equal outcomes. The target load rate for each SD pair is proportional to its probability multiplied by the

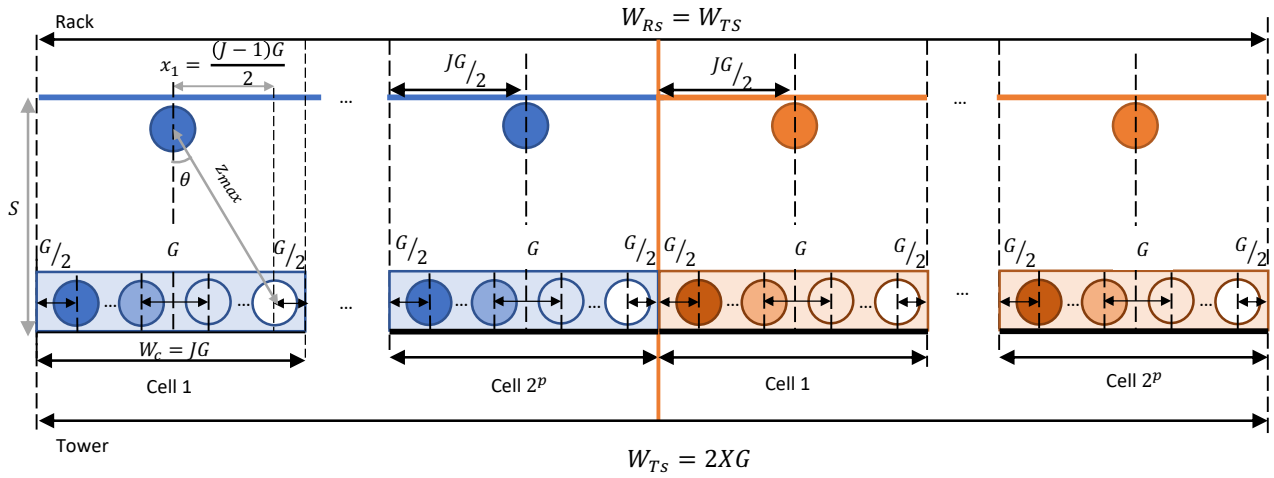

Fig. 17. Beam-steering layout: A top view between a single side of the rack and a single side of the tower, where J is set to be even.

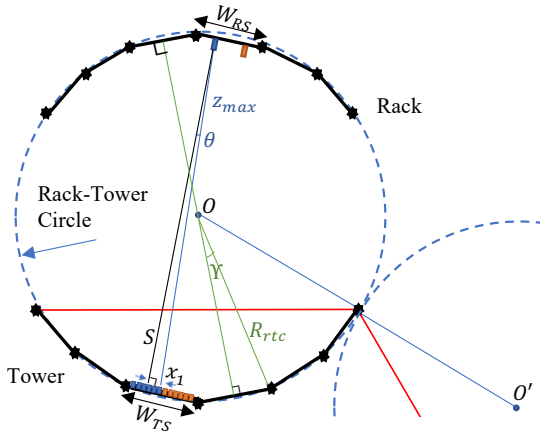

Fig. 18. Feasibility criteria for horizontal limited layout ($J = 6$, $p = 0$).

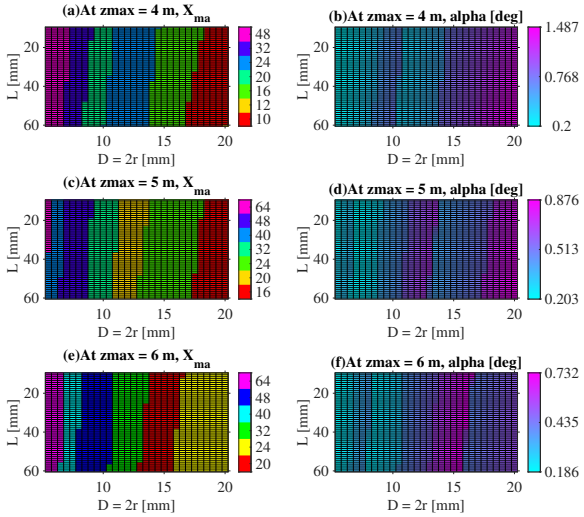

Fig. 19. Heatmap of maximum achievable X (denoted as X_{ma}) and required angle α by actuator.

total load rate $= sum(flow\_size)/sum(event\_time)$ in the network. Starting from the SD pairs furthest from their targets, Trafpy packs flows to each pair. However, Trafpy ensures that any source or destination does not exceed its maximum capacity, by capping it at 1.0 load individually and uniformly redistributing any excess flows into others. This leads to a near uniform distribution as the overall load η approaches 1.0, regardless of the original skewness (see Fig.12). More details on this can be found in [53].

The DSU scheduler is a revised and to be submitted version of a previous hardware scheduler in PULSE [39] and its detail working mechanism is beyond the scope of this work.

APPENDIX D
PRACTICAL CONSIDERATIONS FOR ACTUATORS

The benefits of using PZTs in FSO switch include: (1) Resolution and repeatability are mainly limited by the electronic driving circuits and DACs. A PZT has a theoretically continuous movement since its displacement arises from the alignment of dipoles in response to an applied electric field with no mechanical friction or backlash [57], [58]. The study in [58, Tab. 2] summarized a list of commercial actuators with resolution down to sub-nm or sub-μrad, sufficient to cover the proposed FSO misalignment tolerance. (2) The fiber-collimator packages could weight from $\sim$30 g [59] to 300 g [60], which can be supported by most actuators up to hundreds of Newton [58, Tab. 2]. (3) Vibration, hysteresis and creep can be well controlled with feedback, feedforward or both controllers [58, Fig. 1] as in commercial products. Although beyond the scope of this paper, we intend to address this issue with proportional–integral–derivative (PID) controller with deep reinforcement learning to optimize PZT parameter tuning in future works. The major trade-off is the resonant frequency (mostly <kHz) of a commercial PZT to reach a peak-to-peak tip displacement τ required as,

$$\tau = \pm L \sin \alpha \,, \tag{10}$$

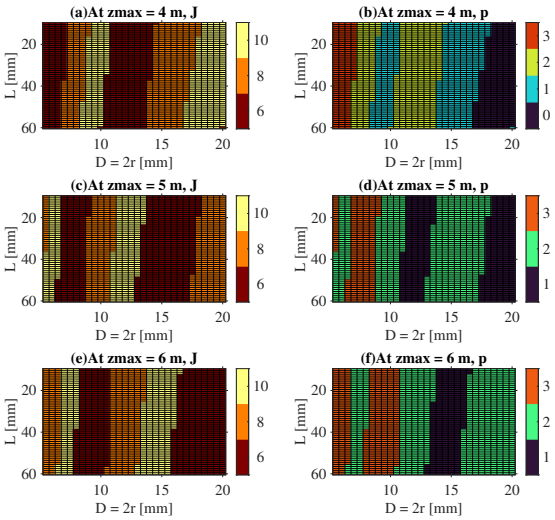

Fig. 20. Heatmap of required J, p to reach the X_{ma} in Fig.19.

where L, α are defined in Fig. 5. This gives $\tau_A = \pm 41.89$ μm, $\tau_B = \pm 32.46$ μm, $\tau_C = \pm 196.31$ μm for case A, B, C (in Table V), respectively. In summary: (1) For FSO-ST, reconfigurability can be solely managed by wavelength tuning with sub-nanosecond (< 900 ps) switching delay using wideband wavelength tunable source (WTS) in [49]. (2) For FSO-BS, reconfigurability depends on both wavelength tuning and actuator switching speed, which is dominant by the latter one at tens of microseconds to a few milliseconds. A possible solution is to pre-schedule the FSO switching before any communication and then remain the topology as static with all reconfigurability accomplished through wavelength tuning once started.

REFERENCES

[1] A. Richter, S. Dris, I. Koltchanov, S. Alreesh, D. Yevseyenko, and E. Sokolov, "Optical interconnects for datacenter links: design and modeling challenges," in *Optical Interconnects XX*, H. Schröder and R. T. Chen, Eds., vol. 11286, International Society for Optics and Photonics. SPIE, 2020, pp. 241 – 251. [Online]. Available: https://doi.org/10.1117/12.2545944

[2] C. Kachris, K. Kanonakis, and I. Tomkos, "Optical interconnection networks in data centers: recent trends and future challenges," *IEEE Communications Magazine*, vol. 51, no. 9, pp. 39–45, 2013.

[3] Cisco, "Cisco global cloud index: Forecast and methodology, 2011–2016," Cisco White Paper, 2011. [Online]. Available: https://www.cisco.com/c/dam/global/en_au/assets/cisco-live/ites2013mel/assets/presentations/Cloud_Index_White_Paper.pdf

[4] K. Ramachandran, R. Kokku, R. Mahindra, and S. Rangarajan, "60 ghz data-center networking: Wireless $\Longrightarrow$ worry less?" *NEC Research Paper*, vol. 1, 01 2008.

[5] T. Chen, X. Gao, and G. Chen, "The features, hardware, and architectures of data center networks: A survey," *Journal of Parallel and Distributed Computing*, vol. 96, pp. 45–74, 2016. [Online]. Available: https://www.sciencedirect.com/science/article/pii/S0743731516300399

[6] N. Hamedazimi, Z. Qazi, H. Gupta, V. Sekar, S. R. Das, J. P. Longtin, H. Shah, and A. Tanwer, "Firefly: A reconfigurable wireless data center fabric using free-space optics," in *Proceedings of the 2014 ACM Conference on SIGCOMM*, ser. SIGCOMM '14. New York, NY, USA: Association for Computing Machinery, 2014, pp. 319–330. [Online]. Available: https://doi.org/10.1145/2619239.2626328

[7] A. S. Hamza, J. S. Deogun, and D. R. Alexander, "Wireless communication in data centers: A survey," *IEEE Communications Surveys & Tutorials*, vol. 18, no. 3, pp. 1572–1595, 2016.

[8] J.-Y. Shin, E. G. Sirer, H. Weatherspoon, and D. Kirovski, "On the feasibility of completely wireless datacenters," in *2012 ACM/IEEE Symposium on Architectures for Networking and Communications Systems (ANCS)*, 2012, pp. 3–14.

[9] S. Kandula, J. Padhye, and V. Bahl, "Flyways to de-congest data center networks," Tech. Rep. MSR-TR-2009-109, August 2009. [Online]. Available: https://www.microsoft.com/en-us/research/publication/flyways-to-de-congest-data-center-networks/

[10] X. Zhou, Z. Zhang, Y. Zhu, Y. Li, S. Kumar, A. Vahdat, B. Zhao, and H. Zheng, "Mirror mirror on the ceiling: Flexible wireless links for data centers," *ACM SIGCOMM Computer Communication Review*, vol. 42, 10 2012.

[11] C. Zhang, F. Wu, X. Gao, and G. Chen, "Free talk in the air: A hierarchical topology for 60 ghz wireless data center networks," *IEEE/ACM Transactions on Networking*, vol. 25, no. 6, pp. 3723–3737, 2017.

[12] Y. Katayama, K. Takano, Y. Kohda, N. Ohba, and D. Nakano, "Wireless data center networking with steered-beam mmwave links," in *2011 IEEE Wireless Communications and Networking Conference*, 2011, pp. 2179–2184.

[13] Y. Cui, S. Xiao, X. Wang, Z. Yang, C. Zhu, X. Li, L. Yang, and N. Ge, "Diamond: Nesting the data center network with wireless rings in 3d space," in *13th USENIX Symposium on Networked Systems Design and Implementation (NSDI 16)*. Santa Clara, CA: USENIX Association, Mar. 2016, pp. 657–669. [Online]. Available: https://www.usenix.org/conference/nsdi16/technical-sessions/presentation/cui

[14] H. Vardhan, N. Thomas, S.-R. Ryu, B. Banerjee, and R. Prakash, "Wireless data center with millimeter wave network," in *2010 IEEE Global Telecommunications Conference GLOBECOM 2010*, 2010, pp. 1–6.

[15] A. Jahid, M. H. Alsharif, and T. J. Hall, "A contemporary survey on free space optical communication: Potential, technical challenges, recent advances and research direction," 2020.

[16] X. Wu, S. Zhang, and A. Özgür, "Stac: Simultaneous transmitting and air computing in wireless data center networks," *IEEE Journal on Selected Areas in Communications*, vol. 34, no. 12, pp. 4024–4034, 2016.

[17] I. K. Son and S. Mao, "A survey of free space optical networks," *Digital Communications and Networks*, vol. 3, no. 2, pp. 67–77, 2017. [Online]. Available: https://www.sciencedirect.com/science/article/pii/S2352864816300542

[18] A. S. Hamza, J. S. Deogun, and D. R. Alexander, "Free space optical data center architecture design with fully connected racks," in *2014 IEEE Global Communications Conference*, 2014, pp. 2192–2197.

[19] J. Mirza, A. Raza, A. Atieh, S. Iqbal, and S. Ghafoor, "Self restorable intra data center interconnect based on multimode fiber and free-space optics," *Optical Engineering*, vol. 60, no. 3, p. 036113, 2021. [Online]. Available: https://doi.org/10.1117/1.OE.60.3.036113

[20] S. Arnon, "Next-generation optical wireless communications for data centers," in *Broadband Access Communication Technologies IX*, B. B. Dingel and K. Tsukamoto, Eds., vol. 9387, International Society for Optics and Photonics. SPIE, 2015, p. 938703. [Online]. Available: https://doi.org/10.1117/12.2075269

[21] S. Zhang, R. Kraemer, B. Pan, X. Xue, K. Prifti, F. Yan, X. Guo, E. Tangdiongga, and N. Calabretta, "Experimental assessment of a novel optical wireless data center network architecture," in *2020 European Conference on Optical Communications (ECOC)*, 2020, pp. 1–4.

[22] A. S. Hamza, S. Yadav, S. Ketan, J. S. Deogun, and D. R. Alexander, "Owcell: Optical wireless cellular data center network architecture," in *2017 IEEE International Conference on Communications (ICC)*, 2017, pp. 1–6.

[23] K. H. Heng, W.-D. Zhong, and T. H. Cheng, "Multipoint free-space optics system for short-range communications between flight platforms," *Appl. Opt.*, vol. 49, no. 2, pp. 258–266, Jan 2010. [Online]. Available: http://opg.optica.org/ao/abstract.cfm?URI=ao-49-2-258

[24] M. Ghobadi, R. Mahajan, A. Phanishayee, N. Devanur, J. Kulkarni, G. Ranade, P.-A. Blanche, H. Rastegarfar, M. Glick, and D. Kilper, "Projector: Agile reconfigurable data center interconnect," in *Proceedings of the 2016 ACM SIGCOMM Conference*, ser. SIGCOMM '16. New York, NY, USA: Association for Computing Machinery, 2016, p. 216–229. [Online]. Available: https://doi.org/10.1145/2934872.2934911

[25] C. Chaintoutis, B. Shariati, A. Bogris, P. V. Dijk, C. G. H. Roeloffzen, J. Bourderionnet, I. Tomkos, and D. Syvridis, "Free space intra-datacenter interconnects based on 2d optical beam steering enabled by

photonic integrated circuits," *Photonics*, vol. 5, no. 3, 2018. [Online]. Available: https://www.mdpi.com/2304-6732/5/3/21

[26] S. Ghafoor, J. Mirza, T. Kousar, and K. K. Qureshi, "A novel 60 gbps bidirectional free space optical link based on a single laser source," *Arabian Journal for Science and Engineering*, vol. 47, no. 11, pp. 14 721–14 729, 2022. [Online]. Available: https://doi.org/10.1007/s13369-022-06975-3

[27] F. El-Nahal, T. Xu, D. AlQahtani, and M. Leeson, "A bidirectional wavelength division multiplexed (wdm) free space optical communication (fso) system for deployment in data center networks (dcns)," *Sensors*, vol. 22, no. 24, 2022. [Online]. Available: https://www.mdpi.com/1424-8220/22/24/9703

[28] M. A. Fernandes, P. P. Monteiro, and F. P. Guiomar, "Single-wavelength terabit fso channel for datacenter interconnects enabled by adaptive pcs," in *2021 Optical Fiber Communications Conference and Exhibition (OFC)*, 2021, pp. 1–3.

[29] D. Kakati and S. C. Arya, "A 640-gbps, 15.2344-b/s/hz full-duplex optical fiber/wireless single-channel coherent communication system using iqm-based dp-256-qam and dsp techniques," *Photonic Network Communications*, vol. 39, no. 1, pp. 26–38, 2020. [Online]. Available: https://doi.org/10.1007/s11107-019-00875-7

[30] X. Huang, X. Xie, J. Song, T. Duan, H. Hu, X. Xu, and Y. Su, "Performance comparison of all-optical amplify-and-forward relaying fso communication systems with ook and dpsk modulations," *IEEE Photonics Journal*, vol. 10, no. 4, pp. 1–11, 2018.

[31] D. D. M.D., S. Z. Sr., D. Y. Sr., and Y. Che, "A new method to handle rack vibration in FSO for data center," in *Thirteenth International Conference on Information Optics and Photonics (CIOP 2022)*, Y. Yang, Ed., vol. 12478, International Society for Optics and Photonics. SPIE, 2022, p. 124783E. [Online]. Available: https://doi.org/10.1117/12.2654822

[32] P. Deng, T. Kane, and O. Alharbi, "Reconfigurable free space optical data center network using gimbal-less MEMS retroreflective acquisition and tracking," in *Free-Space Laser Communication and Atmospheric Propagation XXX*, H. Hemmati and D. M. Boroson, Eds., vol. 10524, International Society for Optics and Photonics. SPIE, 2018, p. 1052403. [Online]. Available: https://doi.org/10.1117/12.2295831

[33] H. P. Kuo, P. Rosenberg, R. Walmsley, S. Mathai, L. Kiyama, J. Straznicky, M. Mclaren, M. Tan, and S.-Y. Wang, "Free-space optical links for board-to-board interconnects," *Applied Physics A*, vol. 95, no. 4, pp. 955–965, 2009. [Online]. Available: https://doi.org/10.1007/s00339-009-5144-z

[34] K. Wang, C. Lim, E. Wong, K. Alameh, S. Kandeepan, and E. Skafidas, "High-speed reconfigurable free-space optical interconnects with carrierless-amplitude-phase modulation and space-time-block code," *Journal of Lightwave Technology*, vol. 37, no. 2, pp. 627–633, 2019.

[35] X. Zhao, L. Zhu, S. Fu, C. Liu, M. Tang, and D. Liu, "Dual-band accelerating beams enabled full duplex free-space optical interconnection," *IEEE Journal of Selected Topics in Quantum Electronics*, vol. 27, no. 1, pp. 1–7, 2021.

[36] V. R. Pamidighantam and R. K. Yeluripati, "Intra-board free-space optical interconnects for data centers," in *Frontiers in Optics + Laser Science 2022 (FIO, LS)*. Optica Publishing Group, 2022, p. JW5A.97. [Online]. Available: https://opg.optica.org/abstract.cfm?URI=FiO-2022-JW5A.97

[37] J. Xue, A. Garg, B. Ciftcioglu, J. Hu, S. Wang, I. Savidis, M. Jain, R. Berman, P. Liu, M. Huang, H. Wu, E. Friedman, G. Wicks, and D. Moore, "An intra-chip free-space optical interconnect," in *Proceedings of the 37th Annual International Symposium on Computer Architecture*, ser. ISCA '10. New York, NY, USA: Association for Computing Machinery, 2010, p. 94–105. [Online]. Available: https://doi.org/10.1145/1815961.1815975

[38] B. Ciftcioglu, R. Berman, S. Wang, J. Hu, I. Savidis, M. Jain, D. Moore, M. Huang, E. G. Friedman, G. Wicks, and H. Wu, "3-d integrated heterogeneous intra-chip free-space optical interconnect," *Opt. Express*, vol. 20, no. 4, pp. 4331–4345, Feb 2012. [Online]. Available: https://opg.optica.org/oe/abstract.cfm?URI=oe-20-4-4331

[39] J. L. Benjamin, T. Gerard, D. Lavery, P. Bayvel, and G. Zervas, "Pulse: Optical circuit switched data center architecture operating at nanosecond timescales," *Journal of Lightwave Technology*, vol. 38, no. 18, pp. 4906–4921, 2020. [Online]. Available: http://jlt.osa.org/abstract.cfm?URI=jlt-38-18-4906

[40] J. L. Benjamin and G. Zervas, "Scaling PULSE Data Center Network Architecture and Scheduling Optical Circuits in Sub-Microseconds," in *2020 Optical Fiber Communications Conference and Exhibition (OFC)*, 2020, pp. 1–3.

[41] N. Soin, S. Anand, and T. Shah, "12 - energy harvesting and storage textiles," in *Handbook of Technical Textiles (Second Edition)*, second edition ed., A. R. Horrocks and S. C. Anand, Eds. Woodhead Publishing, 2016, pp. 357–396. [Online]. Available: https://www.sciencedirect.com/science/article/pii/B9781782424659000124

[42] HUBER+SUHNER-POLATIS, "Triplet fiber optic collimators/couplers," Available at https://www.polatis.com/polatis-all-optical-switch-technology-lowest-loss-highest-performance-directlight-beam-asp.

[43] C. Deakin, M. Enrico, N. Parsons, and G. Zervas, "Design and analysis of beam steering multicore fiber optical switches," *Journal of Lightwave Technology*, vol. 37, no. 9, pp. 1954–1963, 2019.

[44] S. A. Self, "Focusing of spherical gaussian beams," *Applied Optics*, vol. 22, no. 5, pp. 658–661, 1983. [Online]. Available: http://ao.osa.org/abstract.cfm?URI=ao-22-5-658

[45] M. I. S. Chowdhury, M. Kavehrad, and W. Zhang, "Cable television transmission over a 1550-nm infrared indoor optical wireless link," *Optical Engineering*, vol. 52, no. 10, p. 100503, 2013. [Online]. Available: https://doi.org/10.1117/1.OE.52.10.100503

[46] K. Yoshida, K. Tanaka, K. Katayama, T. Tsujimura, and Y. Azuma, "Collimator focus adjustment for free space optics system using single-mode optical fibers," in *2009 ICCAS-SICE*, 2009, pp. 1338–1341.

[47] D. Marcuse, "Loss analysis of single-mode fiber splices," *The Bell System Technical Journal*, vol. 56, no. 5, pp. 703–718, 1977.

[48] T. S. Khwaja and S. A. Reza, "Low-cost gaussian beam profiling with circular irises and apertures," *Appl. Opt.*, vol. 58, no. 4, pp. 1048–1056, Feb 2019. [Online]. Available: http://opg.optica.org/ao/abstract.cfm?URI=ao-58-4-1048

[49] T. Gerard, C. Parsonson, Z. Shabka, B. Thomsen, P. Bayvel, D. Lavery, and G. Zervas, "Ai-optimised tuneable sources for bandwidth-scalable, sub-nanosecond wavelength switching," *Opt. Express*, vol. 29, no. 7, pp. 11 221–11 242, Mar 2021. [Online]. Available: http://opg.optica.org/oe/abstract.cfm?URI=oe-29-7-11221

[50] C. W. F. Parsonson, Z. Shabka, W. K. Chlupka, B. Goh, and G. Zervas, "Optimal control of soas with artificial intelligence for sub-nanosecond optical switching," *Journal of Lightwave Technology*, vol. 38, no. 20, pp. 5563–5573, 2020.

[51] J. L. Benjamin, C. W. F. Parsonson, and G. Zervas, "Benchmarking Packet-Granular OCS Network Scheduling for Data Center Traffic Traces," in *OSA Advanced Photonics Congress 2021*. Optica Publishing Group, 2021, p. NeW3B.3. [Online]. Available: http://opg.optica.org/abstract.cfm?URI=Networks-2021-NeW3B.3

[52] J. L. Benjamin, A. Ottino, C. W. F. Parsonson, and G. Zervas, "Traffic tolerance of nanosecond scheduling on optical circuit switched data center network," in *2022 Optical Fiber Communications Conference and Exhibition (OFC)*, 2022, pp. 1–3.

[53] C. W. Parsonson, J. L. Benjamin, and G. Zervas, "Traffic generation for benchmarking data centre networks," *Optical Switching and Networking*, vol. 46, p. 100695, 2022. [Online]. Available: https://www.sciencedirect.com/science/article/pii/S1573427722000315

[54] H. Kaushal and G. Kaddoum, "Free space optical communication: Challenges and mitigation techniques," 2015. [Online]. Available: https://arxiv.org/abs/1506.04836

[55] E. Lundström, G. Brodin, J. Lundin, M. Marklund, R. Bingham, J. Collier, J. T. Mendonça, and P. Norreys, "Using high-power lasers for detection of elastic photon-photon scattering," *Phys. Rev. Lett.*, vol. 96, p. 083602, Mar 2006. [Online]. Available: https://link.aps.org/doi/10.1103/PhysRevLett.96.083602

[56] M. Sangal, C. H. Keitel, and M. Tamburini, "Observing light-by-light scattering in vacuum with an asymmetric photon collider," *Phys. Rev. D*, vol. 104, p. L111101, Dec 2021. [Online]. Available: https://link.aps.org/doi/10.1103/PhysRevD.104.L111101

[57] Z. Chi and Q. Xu, "Recent advances in the control of piezoelectric actuators," *International Journal of Advanced Robotic Systems*, vol. 11, no. 11, p. 182, 2014.

[58] D. Sabarianand, P. Karthikeyan, and T. Muthuramalingam, "A review on control strategies for compensation of hysteresis and creep on piezoelectric actuators based micro systems," *Mechanical Systems and Signal Processing*, vol. 140, p. 106634, 2020. [Online]. Available: https://www.sciencedirect.com/science/article/pii/S0888327020300200

[59] Thorlabs, "Triplet fiber optic collimators/couplers," Available at https://www.thorlabs.com/newgrouppage9.cfm?objectgroup_id=5124.

[60] M. laser systems.Inc, "Adjustable fiber collimators," Available at http://www.microlaser.com/FiberOptic/FiberCollimators.html.